








Grating designs for cone beam edge illumination X-ray phase contrast imaging: a simulation study

PIETER-JAN VANTHIENEN,^{1,2,*}  JONATHAN SANCTORUM,^{1,2} 
BEN HUYGE,^{1,2} NATHANAËL SIX,^{1,2}  JAN SIJBERS,^{1,2} 
AND JAN DE BEENHOUWER^{1,2} 

¹*imec-Vision Lab, Dept. of Physics, University of Antwerp, Universiteitsplein 1, 2610 Antwerpen, Belgium*

²*DynXlab: Center for 4D Quantitative X-ray Imaging and Analysis, Universiteitsplein 1, 2610 Antwerpen, Belgium*

**pieter-jan.vanthienen@uantwerpen.be*

Abstract: Edge illumination is an emerging X-ray phase contrast imaging technique providing attenuation, phase and dark field contrast. Despite the successful transition from synchrotron to lab sources, the cone beam geometry of lab systems limits the effectiveness of using conventional planar gratings. The non-parallel incidence of X-rays introduces shadowing effects, worsening with increasing cone angle. To overcome this limitation, several alternative grating designs can be considered. In this paper, the effectiveness of three alternative designs is compared to conventional gratings using numerical simulations. Improvements in flux and contrast are discussed, taking into account practical considerations concerning the implementation of the designs.

© 2023 Optica Publishing Group under the terms of the [Optica Open Access Publishing Agreement](#)

1. Introduction

Edge illumination (EI) [1] is an X-ray phase-contrast imaging technique that allows imaging a sample with three complementary contrasts: attenuation, phase and dark field contrast. EI is well-suited for laboratory X-ray phase contrast set-ups [2], because it does not require coherent radiation, has a relatively simple set-up, can easily be scaled up in size, and is robust to mechanical vibrations or imperfections [3]. These advantages create potential for EI in various applications, such as medical imaging [4], security [5], historical studies [6] and materials science [7].

In Fig. 1, a typical EI-XCT set-up is depicted schematically. Compared to a conventional X-ray scanning set-up, composed of a source, sample stage and detector, two additional optical components are added: the sample grating and the detector grating [8]. A conventional EI-grating consists of highly absorbing material with periodic apertures. The sample grating is positioned in front of the sample to split the X-ray cone-beam into beamlets. The detector grating is positioned in front of the detector to create insensitive regions between adjacent pixels on the detector, which allows to measure changes in direction of the beamlets. While most edge illumination set-ups use planar gratings with rectangular and equally wide apertures [9,10], alternative grating designs have been proposed in literature. Examples of such designs include L-shaped apertures, which allow to measure 2D refraction sensitivity [11], skipped gratings, which avoid pixel cross-talk [12] and asymmetric gratings, which allow single shot acquisitions [13]. These alternative grating designs have in common that they are all planar and have a regular pattern of identical apertures, with aperture edges parallel to the optical axis.

EI finds its origin in synchrotron radiation experiments with parallel beam sources [14], but has gradually evolved towards lab systems [8]. Although such lab systems, as opposed to synchrotron facilities, traditionally do not generate parallel beam illumination, the gratings required for EI are most often still designed under the assumption of a parallel beam. In systems with relatively small

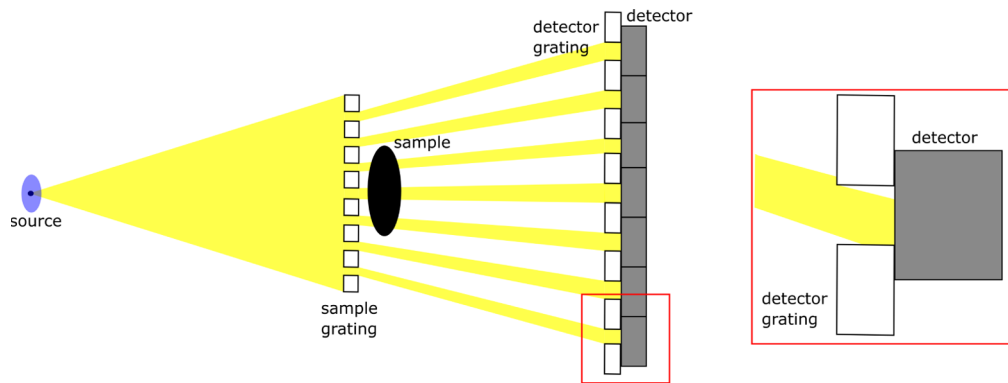


Fig. 1. An EI set-up with conventional gratings and a cone-beam source, showing shadowing.

cone angles, this assumption remains approximately valid, justifying the use of planar gratings. For increasing cone angles, however, the assumption of parallel beam illumination becomes increasingly invalid and a shadowing effect arises [15]. Indeed, while the grating apertures are designed to allow passage to photons travelling parallel to the optical axis, cone beam X-rays might deviate significantly from such a trajectory. Deviating X-rays are likely to hit the aperture edges before they pass the gratings, preventing them from reaching the detector. This geometrical mismatch is perceived as a shadow in the detector plane (hence the shadowing effect) and is also referred to as angular filtration [16]. The larger the deviation from a parallel trajectory, the stronger this effect, as illustrated in Fig. 1. As a consequence, an intensity decrease towards the detector edge can be observed. Studying shadowing and reducing its effect is important to improve cone-beam based EI for multiple reasons. The shadow effect leads to a loss in X-ray flux, decreasing the signal-to-noise ratio away from the center of the detector. It also restricts the field of view (FOV), as for very high angles of incidence photons will no longer be able to travel through the aperture. Shadowing also restricts the aperture width and thickness of the grating, as the severity of the effect is higher for thicker and narrower apertures. While decreasing the grating thickness and increasing the aperture width reduces the effect [17], this comes at the cost of a lower beamlet quality and poorer resolution, respectively.

The shadow effect can be reduced using more advanced grating geometries. Such grating geometries have been tested for grating-based interferometry (GBI) phase contrast imaging set-ups [18]. Both GBI and EI require gratings in the set-up, but the grating pitch is approximately an order of magnitude smaller for GBI in order to generate interference patterns. EI is, in contrast to GBI, a non-interferometric method detecting refraction effects. Examples of alternative grating designs for GBI include curved gratings [19–22], modulated tilting gratings [23,24] and combinations of gratings [25,26]. These alternative gratings are introduced in GBI to increase the FOV. Although similarities in the set-up geometry suggest that EI cone beam imaging would also benefit from more dedicated grating designs, to the best of our knowledge, no comparative studies exist other than our own preliminary work [27], where we compared the X-ray flux of three alternative gratings using Monte-Carlo (MC) simulations.

In this paper, we further extend our simulation work in order to perform an in-depth analysis of the effects on image contrast of three alternative grating geometries, comparing them to conventional gratings. The shared main objective of the alternative grating designs under investigation is the extension to larger zooming factors, without suffering from the shadowing effect. Here, MC simulations are used to evaluate the performance based on unprocessed illumination profiles as well as retrieved phase and attenuation contrast data. To complete our

discussion, the simulation results are complemented with practical considerations concerning the implementation of the alternative designs.

2. Methodology

2.1. Edge illumination

A typical set-up for EI with a cone-beam source is shown in Fig. 1. The X-ray cone-beam is separated into multiple beamlets by the sample grating. As the beamlets traverse the sample, they are attenuated and refracted. The detector grating creates insensitive regions between adjacent detector pixels. Due to the aperture sizes of the gratings, EI can be described using the ray-optical approach, where phase effects are represented by refraction of X-rays in an object [28–30]. The gratings transform refraction effects into intensity modulations at the detector, thereby providing phase-sensitivity. This modulated signal contains information from both attenuation and refraction, which can be separated using phase-stepping. In phase-stepping, the intensity at every pixel is measured while shifting the sample grating. These consecutive measurements result in the construction of the so-called illumination curve (IC) [31,32]. An IC constructed by five phase-steps is shown in Fig. 2.

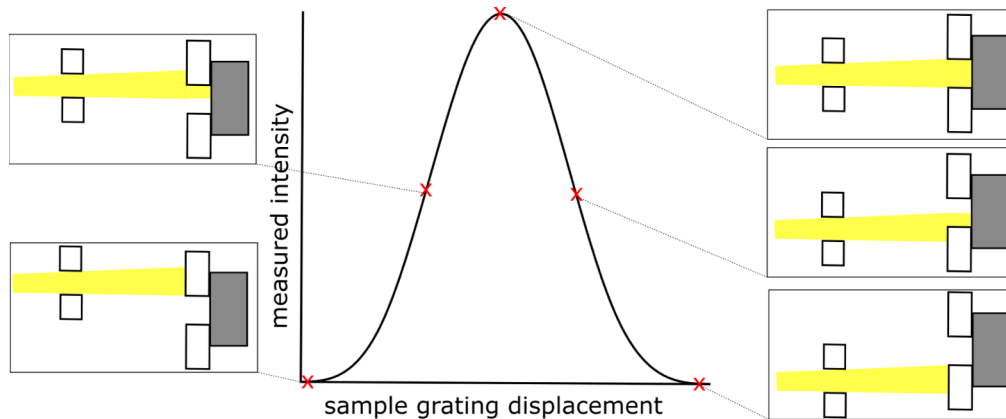


Fig. 2. An IC constructed by five phase-steps. The intensity is measured for different sample grating displacements and a Gaussian curve is fitted to the data points.

Comparing the ICs of a scan without sample (the flat field) and a scan with sample allows one to separate the refraction from the attenuation contrast. The attenuation contrast is retrieved from the difference in area under the ICs. Phase contrast is retrieved from the difference in position of the maxima of the ICs. When three or more phase-steps are measured, a third type of contrast can be obtained, called dark field contrast [7]. Dark field contrast originates from ultra-small angle scattering and is obtained from the broadening of the IC. The three different types of contrast are illustrated in Fig. 3.

2.2. Grating design

The four grating geometries that are studied in this paper are depicted in Fig. 4. The first design is a conventional planar grating (Fig. 4(a)). To reduce shadowing while using conventional gratings, folded gratings are studied as second design, where two conventional gratings are rotated relative to the detector (Fig. 4(b)). The third design being studied is a curved grating (Fig. 4(c)). Curved gratings are sometimes used in GBI, created by pressing conventional gratings into a curved mold, resulting in grating bars with rectangular sections, as shown in Fig. 5(a). The sections of curved gratings discussed in this paper however, are annular sectors, as shown in Fig. 5(b).

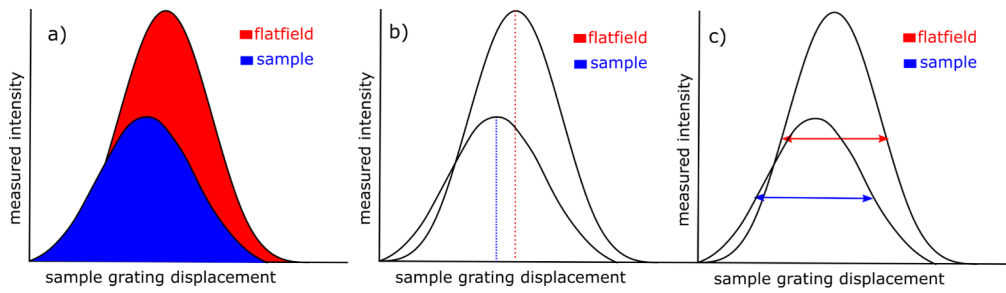


Fig. 3. The 3 different contrast types that can be derived from IC comparison. **a)** Attenuation contrast **b)** phase contrast **c)** dark field contrast.

Since all grating apertures of curved gratings are perfectly parallel to the local beam direction, this design is expected to eliminate shadowing. The fourth and last design is a sheared grating (Fig. 4(d)), where the aperture edges of the curved gratings are projected on a planar surface.

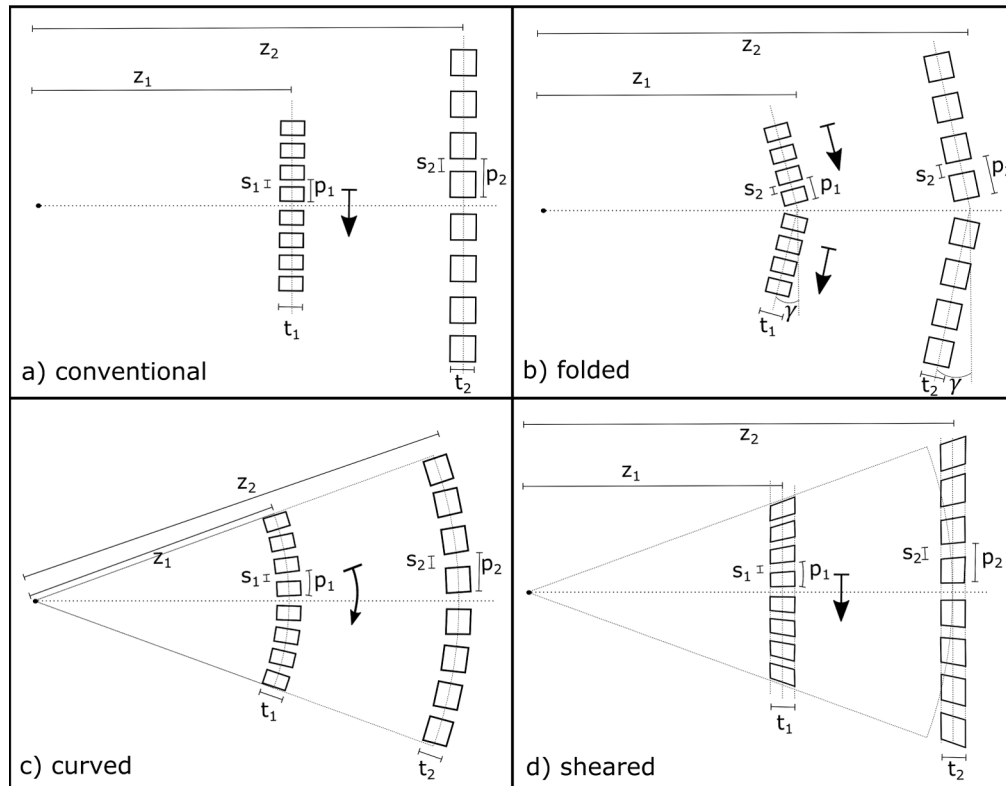


Fig. 4. The different grating geometries studied in this paper. The arrows show the direction of phase-stepping.

The geometrical parameters of the conventional gratings are based on the EI set-up that is installed on the FleXCT scanner [17,33,34] at Imec-Vision Lab, University of Antwerp. For the other grating designs, appropriate geometrical parameters were assigned in order to ensure the same projected pitch at the detector plane and correct magnification at perfect alignment. The parameters of the grating designs are listed in Table 1. A complete mathematical description

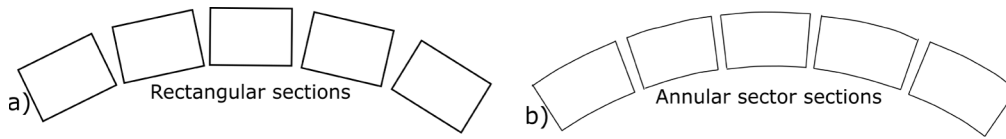


Fig. 5. The sections of curved gratings used in GBI (a) and in this study (b).

of the grating parameters can be found in [Supplement 1](#), section 1. For curved gratings, the same parameters as conventional gratings can be used, because the magnification remains the same. The tilt angle (γ) of folded gratings is chosen to ensure minimal shadowing for the central aperture of each composing grating. The magnification factor at the central apertures is different compared to conventional gratings, which requires a slightly altered period. For sheared gratings, the period and aperture vary across the FOV, as their apertures are projected onto a planar surface.

Table 1. The geometrical parameters for each grating design.

Geometrical parameter	Conventional	Folded	Curved	Sheared
Source-sample grating distance (z_1)	1200 mm	1200 mm	1200 mm	1200 mm
Source-detector grating distance (z_2)	1793.64 mm	1793.64 mm	1793.64 mm	1793.64 mm
Thickness of sample grating (t_1)	225 μm	225 μm	225 μm	225 μm
Thickness of detector grating (t_2)	225 μm	225 μm	225 μm	225 μm
Aperture of sample grating (s_1)	20 μm	20 μm	20 μm	19.88 μm -20.24 μm
Aperture of detector grating (s_2)	30 μm	29.95 μm	30 μm	29.82 μm -30.35 μm
Period of sample grating (p_1)	100 μm	99.8 μm	100 μm	99.4 μm -101.18 μm
Period of detector grating (p_2)	149.47 μm	149.45 μm	149.47 μm	149.12 μm -151.8 μm

While the direction of phase-stepping of conventional and sheared gratings is perpendicular to the optical axis and grating bars, this is different for the curved and the folded grating. In the case of curved gratings, the sample grating rotates around the source. In case of the folded grating the two gratings translate independently of each other, along the direction perpendicular to their grating bars respectively. The direction of phase-stepping is also indicated in [Fig. 4](#) for each grating design.

2.3. Simulation methodology

The performance of the alternative grating geometries is evaluated by means of simulations in GATE [35], an MC software-platform based on Geant4 [36]. GATE is a well-established tool to simulate radiographs, CT-scans, PET and SPECT. In GATE-simulations, X-rays are simulated as photon particles travelling through a user-defined set-up. A simple set-up containing a source, sample, and a detector results in an attenuation contrast image. Recently, X-ray refraction was added to a customized version of GATE [37], enabling EI-simulations by adding gratings to the simulation set-up. In this work, however, a virtual grating approach was used to model the gratings [38]. In the virtual grating approach, the gratings are defined as virtual volumes, and the intersections of every photon with the virtual volume are saved to the output of the simulation. The intersection points are used in the following step to simulate the effect of different grating geometries in a set-up with the same sample, source and detector. To achieve this, a grating geometry inside this virtual volume is defined. If a photon travels through grating bar material, its distance within the grating bar is calculated and its attenuation is determined using the Beer-Lambert law. Defining the gratings after the MC simulation allows to use only one MC simulation for all the different geometries. This saves a significant amount of time when different

geometries or large parameter spaces are studied. An example of a GATE-macro is included in [Supplement 1](#), section 2.

3. Experiments

The set-up for the EI-simulations is adapted to the FleXCT scanner [33] at imec Vision Lab, University of Antwerp. A source-to-detector distance (SDD) of 1800 mm and a grating magnification factor of 3/2 is used in the simulations. The source is a polychromatic (60kV) cone-beam source with a finite spot-size of $34 \times 10 \mu\text{m}^2$. For a line-detector consisting of 3201 pixels of $150 \mu\text{m}$, this geometry results in a cone angle of 15.2° , which is high enough to notice the shadow effect using conventional gratings. To sufficiently block incoming X-rays, gold was chosen as absorbing material for the grating bars. Each MC-simulation in GATE uses $2 \cdot 10^8$ photons and the IC is sampled at 5 phase-steps for every flat field and projection.

3.1. Flat field intensity

As a first experiment, the intensity loss induced by the shadow effect was studied, by comparing the unprocessed flat field profiles of the different grating designs. One MC simulation was run, without a sample, but with virtual volumes. Using the virtual grating approach, a flat field profile at 5 phase-steps was acquired for each grating design.

3.2. Attenuation and phase contrast

The effect of shadowing on phase and attenuation contrast for an increasing cone angle was investigated in a second experiment, where both contrast profiles were simulated for a row of aluminum cylinders, as shown in Fig. 6(a). The radius of the cylinders was 3mm and they were positioned with a distance of 4mm between the edges of two consecutive cylinders. Compared to the flat field intensity experiment, this experiment required an additional MC simulation, including a phantom. The virtual grating approach was used to calculate projection data of 5 phase-steps for each grating geometry, allowing to construct an IC of every pixel with and without the sample. The fitting parameters of these ICs were used to retrieve a phase contrast and attenuation contrast profile for each geometry.

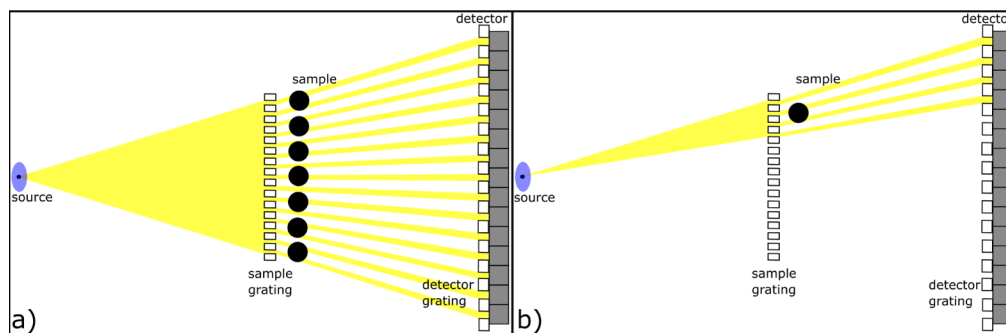


Fig. 6. The set-up of the experiments. a) Attenuation and phase contrast. b) Contrast precision and p2p-CNR.

3.3. Contrast precision

In order to test the precision of the contrast close to the edge of the FOV, the mean and variance of the contrasts was calculated from repeated MC experiments. For every geometry, 50 different MC simulations were performed with and without a sample. This sample, the same aluminum cylinder used in the previous experiment, was placed at the edge of the FOV, corresponding to a

high cone angle, as shown in Fig. 6(b). For each simulation, the phase and attenuation contrast was retrieved. The mean and variance of the contrasts were calculated on a pixel-by-pixel basis including all 50 simulations.

3.4. Peak-to-peak contrast-to-noise ratio

In the fourth experiment, the different grating designs are compared based on the peak-to-peak contrast-to-noise ratio (p2p-CNR) [17]. The p2p-CNR was calculated by dividing the difference between the two refraction peaks at the edges of the same aluminum cylinder by the variance of the signal. This experiment made use of the same 50 phase-contrast profiles discussed in the contrast precision experiment, where the aluminum cylinder was kept at the same position, as shown in Fig. 6(b).

4. Results

4.1. Flat field intensity

The simulated flat field profiles are shown in Fig. 7, their corresponding average and peak intensity values are shown in Table 2. In the simulation with conventional gratings (Fig. 7(a)), shadowing is clearly visible, as the measured intensity decreases towards the outer pixels. A similar profile can also be observed in the flat field of the folded design (Fig. 7(b)), showing two peaks instead of one. This can be understood by considering that folded gratings consist of two conventional gratings. The two maxima in the folded grating flat field profiles reach the same height as the maximum in the conventional grating flat field profile. While the measured intensity at the center is lower when using folded gratings, the overall intensity is higher. This implies that using folded gratings results, on average, in decreased shadowing. In the flat field profile of curved gratings (Fig. 7(c)), the previously discussed shadowing effect is absent. Moreover, the measured intensity is, apart from noise, equal for every pixel. This result demonstrates that the curved gratings completely eliminate shadowing. Another interesting result is that a highly similar profile is acquired in the simulation with sheared gratings (Fig. 7(d)). When perfectly aligned, the projected beamlets are identical for the sheared and curved gratings. This perfect agreement is, however, not preserved when shifting the sheared grating and rotating the curved grating. The average intensity measured with sheared gratings is slightly lower than with curved gratings, but the difference is very small. This suggests that the sheared gratings can serve as a good approximation for curved gratings.

Table 2. The average and peak intensity for each grating at the different phase-steps.

phase-step	Average intensity				Peak intensity			
	conventional	folded	curved	sheared	conventional	folded	curved	sheared
-15 μm	468	755	1812	1811	1909	1890	2045	2027
-7.5 μm	1556	2635	4304	4304	4404	4476	4631	4618
0 μm	2461	4089	5873	5865	6012	6016	6284	6285
7.5 μm	1556	2635	4303	4302	4402	4397	4598	4581
15 μm	467	755	1811	1810	1871	1934	2018	1992

4.2. Attenuation and phase contrast

Attenuation and differential phase contrast profiles of a row of aluminum cylinders are shown in Fig. 8(a),(b). It is immediately clear that the attenuation contrast of identical cylinders varies over the FOV, although this is expected to remain constant. More specifically, it substantially decreases towards the edges of the FOV. This artefact can be explained by the beam hardening

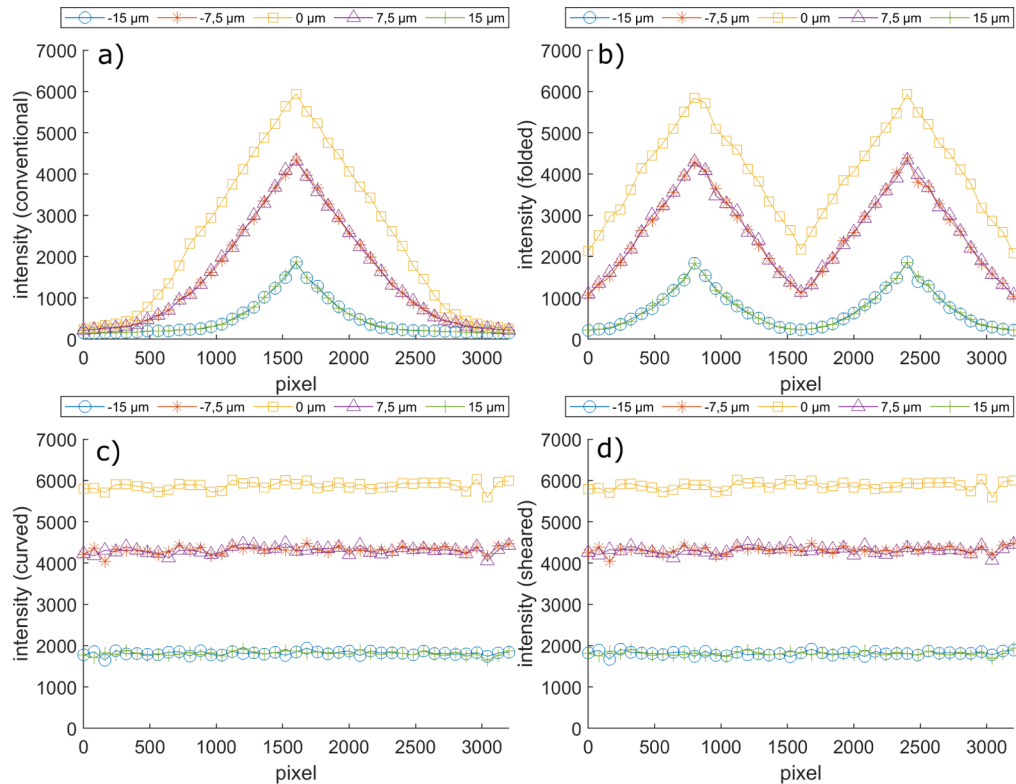


Fig. 7. The flat field for each phase-step per geometry. **a)** conventional, **b)** folded, **c)** curved, **d)** sheared.

resulting from the partially transmitting grating bars. At higher angles of incidence, low-energy photons are absorbed while high-energy photons are still able to penetrate through the grating bars. As a result, the effective spectrum around the central aperture differs from that for an aperture towards the edge. When a phantom is introduced, the difference in photon energy will lead to a difference in attenuation, although the objects are identical. This hypothesis is verified by repeating the same simulation with a monochromatic source. If all the photons have the same energy, the artefact is absent, and the attenuation remains constant throughout the FOV. Results of such a monochromatic simulation can be found in [Supplement 1](#), section 3.

The attenuation and phase contrast towards the outer cylinders appears noisier compared to the center. Moreover, starting from a cone angle of 6.2° , the different cylinders can no longer be resolved in the phase contrast. Indeed, due to the severely decreased intensity towards the edges of the FOV, the IC measurements become noisy. This results in low quality fits, obscuring the cylinders in the phase contrast.

Figure 8(c)-(h) show the attenuation and phase contrast for the same row of cylinders with alternative gratings. It can be observed that the described beam hardening artefact is eliminated when curved or sheared gratings are used. The artefact is still visible with folded gratings, but the effect is reduced. Compared to conventional gratings, the attenuation and phase contrasts show less noise towards the outer pixels. Moreover, using alternative gratings allows one to resolve the outer cylinders in the phase contrast profile.

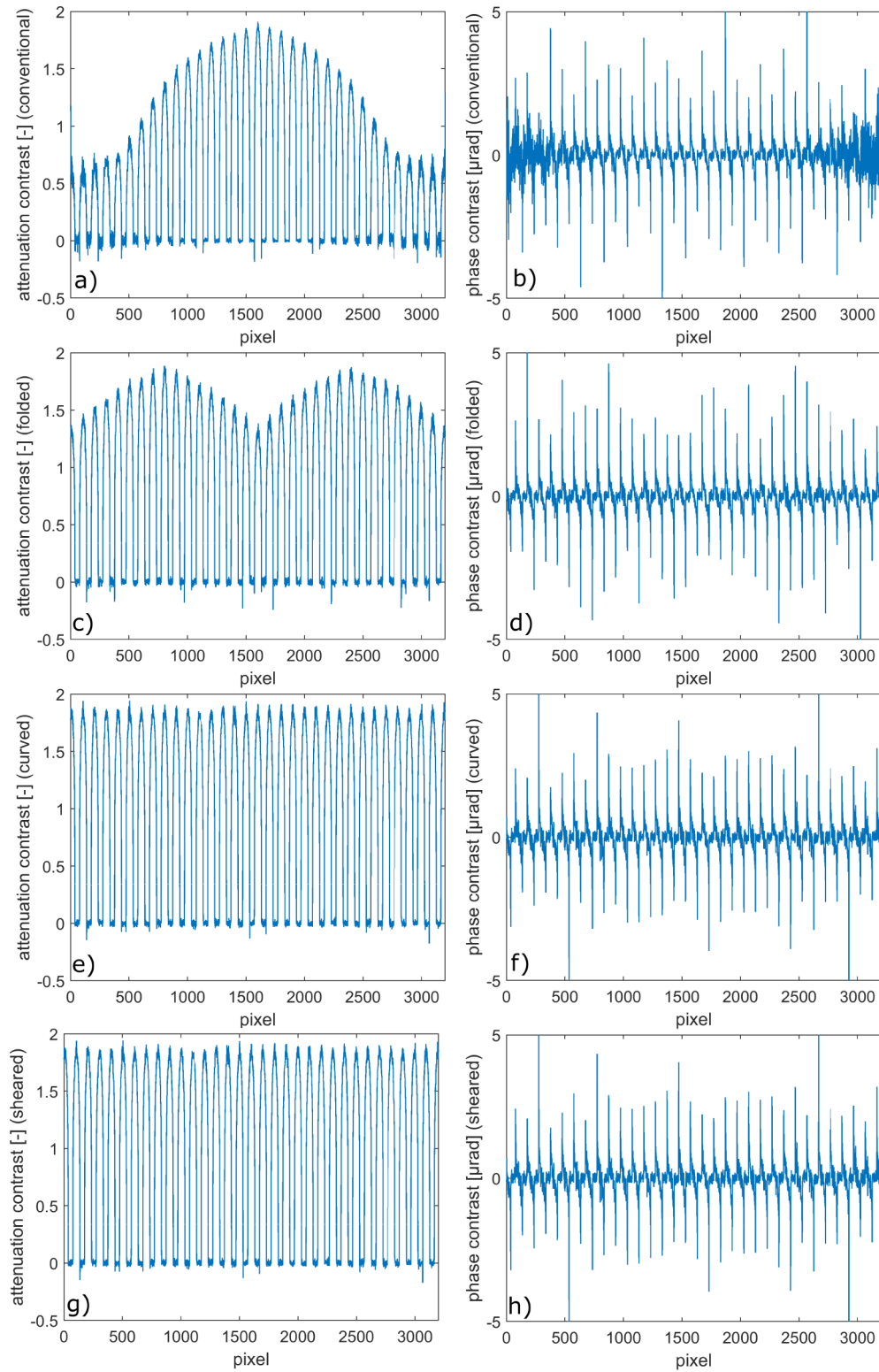


Fig. 8. The attenuation contrast and phase contrast of a row of aluminum cylinders using conventional (a,b) folded (c,d), curved (e,f) and sheared (g,h) gratings.

4.3. Contrast precision

Figure 9 shows the mean and variance of the attenuation contrast of the aluminum cylinder for every pixel. On average, the contrast is the highest for sheared and curved gratings. For folded gratings, the average attenuation contrast is slightly lower, but still higher than the average contrast using conventional gratings. The decreased attenuation contrast in the aluminum cylinder using folded and conventional gratings results from the effect described in the previous section. Comparing the variance of the attenuation contrast leads to similar conclusions with respect to contrast precision. Curved and sheared gratings result in the lowest variance, below folded gratings, which still perform significantly better than conventional gratings. The difference in attenuation contrast variance seems related to X-ray flux, because it corresponds to the flat field intensity at high cone-angles.

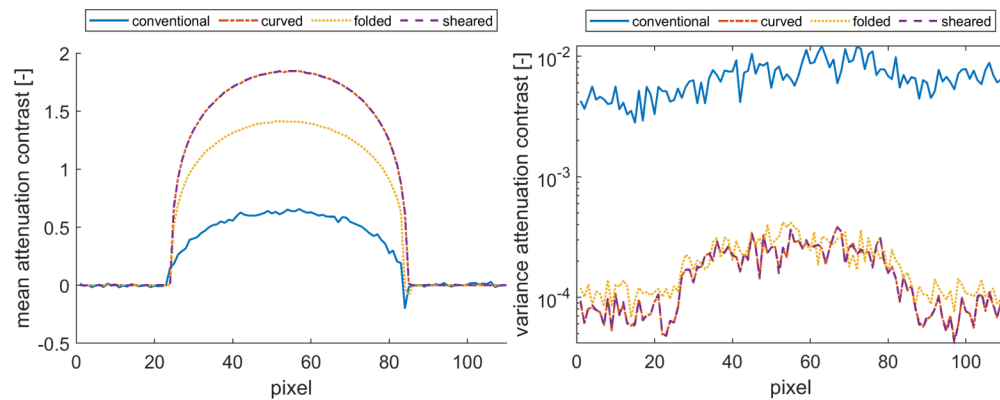


Fig. 9. The mean and variance of attenuation contrast of an aluminum cylinder at the edge of the FOV over 50 simulations, measured at each of its surrounding pixels. Different colors and line styles depict different geometries.

The mean and variance of the phase contrast are shown in Fig. 10. Phase contrast is formulated in terms of refraction angles. Apart from the exact edge positions, the mean phase contrast is similar for the different geometries. At the edges however, the phase contrast peaks are higher when sheared and curved gratings are used, compared to folded and conventional gratings. When the gratings are evaluated on phase contrast variance, conventional gratings show the lowest performance. As opposed to attenuation contrast, folded gratings seem to result in the lowest phase contrast variance. Due to the larger flux, however, a lower variance would be expected for curved and sheared gratings. It is easily tested that a reduced flux results in a higher variance, by reducing the number of photons in the simulation by 50%. Performing this experiment resulted in a clear increase in variance by a factor of 2. Hence, as Table 2 clearly shows that the average recorded intensity is lower for folded gratings, a higher variance would be expected. An explanation is that shadowing causes a narrower beamlet, which can increase the angular sensitivity [39], which in the case of folded gratings outweighs the reduced flux.

4.4. Peak-to-peak contrast-to-noise ratio

In Table 3 the p2p-CNR is shown for the different grating geometries. Results show that the p2p-CNR is consistently the highest when curved and sheared gratings are used. The simulation with folded gratings results shows slightly lower p2p-CNR, but still significantly higher than that of conventional gratings.

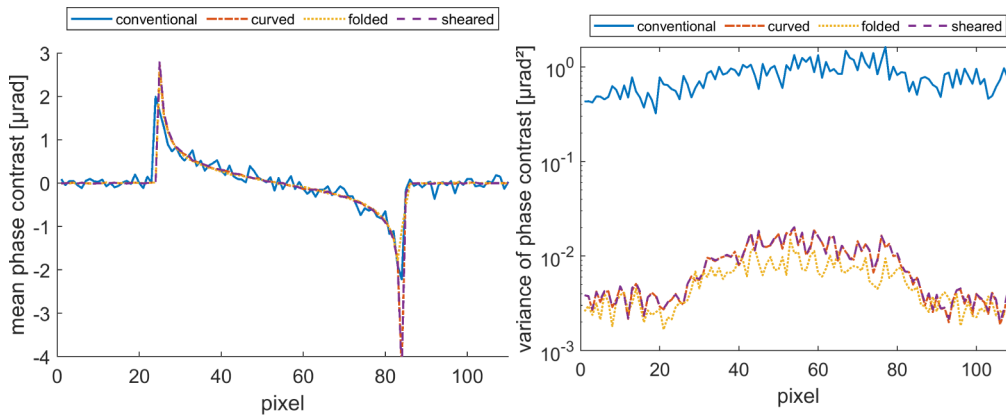


Fig. 10. The mean and variance of phase contrast of an aluminum cylinder at the edge of the FOV over 50 simulations, measured at each of its surrounding pixels. Different colors and line styles depict different geometries.

Table 3. The p2p-CNR ratio of the phase contrast profile for 50 simulations.

	conventional	folded	curved	sheared
p2p-CNR(10^6)	$2,7 \pm 0,6$	$7,4 \pm 0,3$	$10,3 \pm 0,2$	$10,1 \pm 0,2$

5. Discussion

The simulation study shows that folded, curved and sheared gratings have several advantages over conventional gratings for cone-beam based EI. Curved gratings give the best results: the intensity loss in the flat fields is the lowest, the beam hardening artefact is absent, the contrast precision is high and the p2p-CNR is the highest. Sheared gratings, however, show comparable results: the flat field intensity and p2p-CNR is only slightly lower compared to curved gratings, the beam hardening and contrast precision is similar. Folded gratings have advantages over conventional gratings, but show lower performance compared to sheared and curved gratings in the simulation study. The intensity loss and beam hardening artefacts are only partly eliminated. While the contrast precision of folded gratings is comparable to that of curved and sheared gratings, the p2p-CNR is noticeably lower.

While the simulation results show that the three alternative gratings offer improvements, they all come with some complications in practical realisation. Choosing an optimal solution requires a trade-off between the performance shown in the simulation study and the challenges of practical realisation. A qualitative comparison of the alternative gratings based on the simulation study and practical realisation is shown in Table 4.

One of the challenges of realising an EI set-up with curved and sheared gratings lies in manufacturing. While curved and sheared gratings have already been manufactured for GBI using lithography [22] and etching [23], there is a significant difference with EI in terms of grating periodicity. Whereas in GBI a single pixel is illuminated by many apertures, a pixel in an EI setup receives illumination from just one aperture. This implies that a local error in the EI grating period has an immediate impact on a macroscopic level, while for GBI gratings it is much more likely that the effect of such an error would be averaged out. This is an advantage of folded gratings, which can be composed of conventional gratings. Folded gratings and sheared gratings have the advantage that an alignment procedure can be implemented that is similar to aligning conventional gratings, by laterally scanning the grating and stopping at the point with the highest intensity [40]. Compared to conventional gratings however, additional simulations are required,

Table 4. A qualitative comparison of the alternative gratings based on the simulation study and practical realisation(1: Most optimal, 3: Least optimal).

		folded	curved	sheared
Simulation study	Flat field intensity	2	1	1
	Phase and attenuation contrast	2	1	1
	Contrast precision	1	1	1
	p2p-CNR	3	1	2
Practical realisation	Manufacturing	1	2	3
	Alignment	1	3	2
	Installation	3	2	1
	Phase-stepping	2	3	1

to model their specific misalignment behaviour. This is different for curved gratings, where a completely new alignment procedure is necessary. Moreover, sheared and curved gratings are designed for a specific location along the optical axis, while folded gratings can be adapted for different locations along the optical axis, which is also beneficial for alignment. Positioning curved and folded gratings in a scanner causes some complications. Curved gratings require a customized curved protection and a flat connection point to hold the gratings. Folded gratings, on the other hand, require a connection and motorized alignment unit for both parts. Folded gratings require that two conventional gratings are positioned next to each other. Due to the protective case, signal loss in the central pixels is hard to avoid. This is not the case for sheared gratings, which can be installed like conventional gratings. Another advantage of sheared gratings is phase-stepping, which is unidirectional, as for phase-stepping with conventional gratings. Phase-stepping with curved or folded gratings is more complicated. Both parts of the folded grating have to move in a different direction, while a curved grating has to rotate around the source position to perform phase-steps.

By complementing the simulation study with the aspects of practical realisation, our results suggest that sheared gratings are most likely the best alternative grating candidate to reduce the shadow effect. The simulation results demonstrate their superiority over folded gratings and their performance is comparable to curved gratings. Based on practical realisation they show advantages over curved gratings and are comparable to folded gratings. Because of their advantages in practical realisation, folded gratings are arguably the second best option.

6. Conclusion

In this paper, the potential of alternative gratings to solve shadowing-related problems in cone beam EI was investigated. Three alternative geometries were studied: curved, sheared, and folded gratings. MC-simulations showed that the three alternative gratings outperform conventional gratings in terms of flux, contrast, precision and p2p-CNR. Complementing the simulation study with some practical considerations, sheared gratings appear to be the most suitable candidate to solve shadowing-related problems in cone beam EI. Implementing such gratings with reduced shadowing allows increasing cone-angles in EI without sacrificing performance, hereby enabling cone-beam EI with a higher zooming factor, allowing imaging with a higher resolution.

Funding. Agentschap Innoveren en Ondernemen (HBC.2020.2159); Interreg Vlaanderen-Nederland (0386); Fonds Wetenschappelijk Onderzoek (11D8319N, 1S46122N, G090020N, G094320N).

Acknowledgments. This research was supported by EU Interreg Flanders - Netherlands Smart*Light (0386), Fonds wetenschappelijk onderzoek (G090020N, G094320N), and Agentschap Innoveren & Ondernemen (Vlaio) (HBC.2020.2159). Nathanaël Six and Ben Huyge have a PhD fellowship of the FWO (11D8319N, 1S46122N).

Disclosures. The authors declare no conflicts of interest.

Data availability. Data underlying the results presented in this paper are not publicly available at this time but may be obtained from the authors upon reasonable request.

Supplemental document. See [Supplement 1](#) for supporting content.

References

1. A. Olivo, "Edge-illumination x-ray phase-contrast imaging," *J. Phys.: Condens. Matter* **33**(36), 363002 (2021).
2. A. Olivo and E. Castelli, "X-ray phase contrast imaging: From synchrotrons to conventional sources," *Rivista del Nuovo Cimento* **37**, 467–508 (2014).
3. T. P. Millard, M. Endrizzi, K. Ignatyev, C. K. Hagen, P. R. T. Munro, R. D. Speller, and A. Olivo, "Method for automatization of the alignment of a laboratory based x-ray phase contrast edge illumination system," *Rev. Sci. Instrum.* **84**(8), 083702 (2013).
4. M. Longo, L. Rigon, F. C. M. Lopez, R. Chen, D. Dreossi, F. Zanconati, and R. Longo, "A simplified edge illumination set-up for quantitative phase contrast mammography with synchrotron radiation at clinical doses," *Phys. Med. Biol.* **60**(3), N21–N34 (2015).
5. K. Ignatyev, P. R. Munro, D. Chana, R. D. Speller, and A. Olivo, "A new generation of x-ray baggage scanners based on a different physical principle," *Materials* **4**(10), 1846–1860 (2011).
6. A. Gibson, K. E. Piquette, and U. Bergmann, *et al.*, "An assessment of multimodal imaging of subsurface text in mummy cartonnage using surrogate papyrus phantoms," *Heritage Sci.* **6**(1), 7 (2018).
7. M. Endrizzi, B. Murat, P. Fromme, and A. Olivo, "Edge-illumination x-ray dark-field imaging for visualising defects in composite structures," *Composite Structures* **134**, 895–899 (2015).
8. A. Olivo and R. Speller, "A coded-aperture technique allowing x-ray phase contrast imaging with conventional sources," *Appl. Phys. Lett.* **91**(7), 074106 (2007).
9. C. K. Hagen, P. C. Diemoz, M. Endrizzi, L. Rigon, D. Dreossi, F. Arfelli, F. C. M. Lopez, R. Longo, and A. Olivo, "Quantitative edge illumination x-ray phase contrast tomography," *Proc. SPIE* **9212**, 921205 (2014).
10. K. Ignatyev, P. R. T. Munro, R. D. Speller, and A. Olivo, "Phase contrast imaging with coded apertures using laboratory-based x-ray sources," in *10TH international conference on X-ray microscopy, vol. 1365 of AIP Conference Proceedings* I. McNulty, C. Eyberger, and B. Lai, eds. (2011), pp. 254–257.
11. G. K. Kallon, M. Wesolowski, F. A. Vittoria, M. Endrizzi, D. Basta, T. P. Millard, P. C. Diemoz, and A. Olivo, "A laboratory based edge-illumination x-ray phase-contrast imaging setup with two-directional sensitivity," *Appl. Phys. Lett.* **107**(20), 204105 (2015).
12. L. Massimi, J. A. Meganck, R. Towns, A. Olivo, and M. Endrizzi, "Evaluation of a compact multicontrast and multiresolution x-ray phase contrast edge illumination system for small animal imaging," *Med. Phys.* **48**(1), 376–386 (2021).
13. M. Endrizzi, A. Astolfo, F. A. Vittoria, T. P. Millard, and A. Olivo, "Asymmetric masks for laboratory-based x-ray phase-contrast imaging with edge illumination," *Sci. Rep.* **6**(1), 25466 (2016).
14. A. Olivo, F. Arfelli, G. Cantatore, R. Longo, R. Menk, S. Pani, M. Prest, P. Poropat, L. Rigon, G. Tromba, E. Vallazza, and E. Castelli, "An innovative digital imaging set-up allowing a low-dose approach to phase contrast applications in the medical field," *Med. Phys.* **28**(8), 1610–1619 (2001).
15. B. Huyge, J. Sanctorem, N. Six, J. De Beenhouwer, and J. Sijbers, "Analysis of flat fields in edge illumination phase contrast imaging," in *2021 IEEE 18th International Symposium on Biomedical Imaging (ISBI)*, (2021), pp. 1310–1313.
16. I. Buchanan, G. Kallon, T. Beckenbach, J. Schulz, M. Endrizzi, and A. Olivo, "Effective modeling of high-energy laboratory-based x-ray phase contrast imaging utilizing absorption masks or gratings," *J. Appl. Phys.* **128**(21), 214503 (2020).
17. J. Sanctorem, N. Six, J. Sijbers, and J. De Beenhouwer, "Augmenting a conventional x-ray scanner with edge illumination-based phase contrast imaging: how to design the gratings," *Proc. SPIE* **12242**, 1224218 (2022).
18. I. Zanette, S. Rutishauser, C. David, F. Pfeiffer, J. Mohr, and T. Weitkamp, "Multidirectional x-ray dark-field imaging with two-dimensional gratings," in *International Workshop on X-ray and Neutron Phase Imaging with Gratings, vol. 1466 of AIP Conference Proceedings* A. Momose and W. Yashiro, eds. (2012), pp. 12–17.
19. Z. Wu, W. Wei, K. Gao, G. Liu, G. Liu, H. Sun, J. Jiang, Q. Wang, Y. Lu, and Y. Tian, "Prototype system of noninterferometric phase-contrast computed tomography utilizing medical imaging components," *J. Appl. Phys.* **129**(7), 074901 (2021).
20. V. Revol, C. Kottler, R. Kaufmann, I. Jerjen, T. Luethi, F. Cardot, P. Niedermann, U. Straumann, U. Sennhauser, and C. Urbana, "X-ray interferometer with bent gratings: Towards larger fields of view," *Nucl. Instrum. Methods Phys. Res., Sect. A* **648**, S302–S305 (2011).
21. Y. Sun, W. Cong, Y. Xi, G. Wang, and S. Pang, "Talbot interferometry with curved quasi-periodic gratings: towards large field of view x-ray phase-contrast imaging," *Opt. Express* **23**(20), 26576–26585 (2015).
22. T. Thuring, S. Haemmerle, S. Weiss, J. Nueesch, J. Meiser, J. Mohr, C. David, and M. Stampanoni, "Compact hard x-ray grating interferometry for table-top phase contrast micro CT," *Proc. SPIE* **8668**, 866813 (2013).
23. Z. Shi, K. Jefimovs, L. Romano, J. Vila-Comamala, and M. Stampanoni, "Laboratory x-ray interferometry imaging with a fan-shaped source grating," *Opt. Lett.* **46**(15), 3693–3696 (2021).
24. Z. Shi, K. Jefimovs, A. La Magna, M. Stampanoni, and L. Romano, "High aspect ratio tilted gratings through local electric field modulation in plasma etching," *Appl. Surf. Sci.* **588**, 152938 (2022).

25. Y. Lei, X. Liu, J. Huang, Y. Du, J. Guo, Z. Zhao, and J. Li, "Cascade talbot-lau interferometers for x-ray differential phase-contrast imaging," *J. Phys. D: Appl. Phys.* **51**(38), 385302 (2018).
26. T. Schröter, F. Koch, P. Meyer, D. Kunka, J. Meiser, K. Willer, L. Gromann, F. De Marco, J. Herzen, P. Noël, A. Yaroshenko, A. Hofmann, F. Pfeiffer, and J. Mohr, "Large field-of-view tiled grating structures for x-ray phase-contrast imaging," *Rev. Sci. Instrum.* **88**(1), 015104 (2017).
27. P.-J. Vanthienen, J. Sanctorem, B. Huyge, N. Six, J. Sijbers, and J. De Beenhouwer, "Alternative grating designs for cone-beam edge illumination x-ray phase contrast imaging," *Proc. SPIE* **12242**, 122420Z (2022).
28. T. P. Millard, M. Endrizzi, P. C. Diemoz, C. K. Hagen, and A. Olivo, "Monte carlo model of a polychromatic laboratory based edge illumination x-ray phase contrast system," *Rev. Sci. Instrum.* **85**(5), 053702 (2014).
29. S. Wilkins, T. Gureyev, D. Gao, A. Pogany, and A. Stevenson, "Phase-contrast imaging using polychromatic hard x-rays," *Nature* **384**(6607), 335–338 (1996).
30. P. R. T. Munro, K. Ignatyev, R. D. Speller, and A. Olivo, "The relationship between wave and geometrical optics models of coded aperture type x-ray phase contrast imaging systems," *Opt. Express* **18**(5), 4103–4117 (2010).
31. L. Massimi, T. Partridge, A. Astolfo, M. Endrizzi, C. K. Hagen, P. R. T. Munro, D. Bate, and A. Olivo, "Optimization of multipoint phase retrieval in edge illumination X-ray imaging A theoretical and experimental analysis," *Med. Phys.* **48**(10), 5884–5896 (2021).
32. A. Olivo and R. Speller, "Modelling of a novel x-ray phase contrast imaging technique based on coded apertures," *Phys. Med. Biol.* **52**(22), 6555–6573 (2007).
33. B. De Samber, J. Renders, T. Elberfeld, Y. Maris, J. Sanctorem, N. Six, Z. Liang, J. De Beenhouwer, and J. Sijbers, "FlexCT: a flexible X-ray CT scanner with 10 degrees of freedom," *Opt. Express* **29**(3), 3438–3457 (2021).
34. B. Huyge, P. Vanthienen, N. Six, J. Sijbers, and J. De Beenhouwer, "Adapting an XCT-scanner to enable edge illumination x-ray phase contrast imaging," in *Proceedings of the 12th Conference on Industrial Computed Tomography (iCT) 2023*, E-Journal of Nondestructive Testing Vol. 28(3) 1-7 (2023).
35. S. Jan, G. Santin, and D. Strul, *et al.*, "GATE: a simulation toolkit for PET and SPECT," *Phys. Med. Biol.* **49**(19), 4543–4561 (2004).
36. S. Agostinelli, J. Allison, and K. Amako, *et al.*, "Geant4-a simulation toolkit," *Nucl. Instrum. Methods Phys. Res., Sect. A* **506**(3), 250–303 (2003).
37. J. Sanctorem, J. De Beenhouwer, and J. Sijbers, "X-ray phase contrast simulation for grating-based interferometry using GATE," *Opt. Express* **28**(22), 33390–33412 (2020).
38. J. Sanctorem, J. Sijbers, and J. De Beenhouwer, "Virtual grating approach for Monte Carlo simulations of edge illumination-based x-ray phase contrast imaging," *Opt. Express* **30**(21), 38695–38708 (2022).
39. P. Diemoz, M. Endrizzi, C. Hagen, T. Millard, F. Vittoria, and A. Olivo, "Angular sensitivity and spatial resolution in edge illumination x-ray phase-contrast imaging," *Nucl. Instrum. Methods Phys. Res., Sect. A* **784**, 538–541 (2015).
40. A. Doherty, L. Massimi, A. Olivo, and M. Endrizzi, "Optimal and automated mask alignment for use in edge illumination x-ray differential-phase and dark-field imaging techniques," *Nucl. Instrum. Methods Phys. Res., Sect. A* **984**, 164602 (2020).